Science Bulletin 70 (2025) 180–186

Contents lists available at ScienceDirect

Science Bulletin

journal homepage: www.elsevier.com/locate/scib

Article

Distinct ultrafast dynamics of bilayer and trilayer nickelate superconductors regarding the density-wave-like transitions

Yidian Li [a], Yantao Cao [b,c], Liangyang Liu [a], Pai Peng [a], Hao Lin [a], Cuiying Pei [d], Mingxin Zhang [d], Heng Wu [e], Xian Du [a], Wenxuan Zhao [a], Kaiyi Zhai [a], Xuefeng Zhang [d], Jinkui Zhao [c], Miaoling Lin [e], Pingheng Tan [e], Yanpeng Qi [d,f,g], Gang Li [d,f,*], Hanjie Guo [c,*], Luyi Yang [a,h,*], Lexian Yang [a,h,*]

[a] State Key Laboratory of Low Dimensional Quantum Physics, Department of Physics, Tsinghua University, Beijing 100084, China
[b] Key Lab for Magnetism and Magnetic Materials of the Ministry of Education, Lanzhou University, Lanzhou 730000, China
[c] Songshan Lake Materials Laboratory, Dongguan 523808, China
[d] School of Physical Science and Technology, ShanghaiTech University and CAS-Shanghai Science Research Center, Shanghai 201210, China
[e] State Key Laboratory of Superlattices and Microstructures, Institute of Semiconductors, Chinese Academy of Sciences, Beijing 100083, China
[f] ShanghaiTech Laboratory for Topological Physics, Shanghai 200031, China
[g] Laboratory of High-resolution Electron Microscopy, ShanghaiTech University, Shanghai 201210, China
[h] Frontier Science Center for Quantum Information, Beijing 100084, China

ARTICLE INFO

Article history:
Received 21 July 2024
Received in revised form 31 August 2024
Accepted 11 October 2024
Available online 17 October 2024

Keywords:
Nickelate superconductors
Density-wave state
Ultrafast dynamics
Electron–phonon coupling
Coherent phonon

ABSTRACT

In addition to the pressurized high-temperature superconductivity, bilayer and trilayer nickelate superconductors $La_{n+1}Ni_nO_{3n+1}$ (n = 2 and 3) exhibit many intriguing properties at ambient pressure, such as orbital-dependent electronic correlation, non-Fermi liquid behavior, and density-wave transitions. Here, using ultrafast reflectivity measurement, we observe a drastic difference between the ultrafast dynamics of the bilayer and trilayer nickelates at ambient pressure. We observe a coherent phonon mode in $La_4Ni_3O_{10}$ involving the collective vibration of La, Ni, and O atoms, which is absent in $La_3Ni_2O_7$. Temperature-dependent relaxation time diverges near the density-wave transition temperature of $La_4Ni_3O_{10}$, while it is inversely proportional to the temperature in $La_3Ni_2O_7$ above ~150 K, suggesting a non-Fermi liquid behavior of $La_3Ni_2O_7$. Moreover, we estimate the electron–phonon coupling constants to be 0.05–0.07 and 0.12–0.16 for $La_3Ni_2O_7$ and $La_4Ni_3O_{10}$, respectively, suggesting a relatively minor role of electron–phonon coupling in the electronic properties of $La_{n+1}Ni_nO_{3n+1}$ at ambient pressure. The relevant microscopic interaction and dynamic information are essential for further studying the interplay between superconductivity and density-wave transitions in nickelate superconductors.

1. Introduction

Many unconventional superconductors exhibit a common interplay with density-wave states in their phase diagrams. The prime examples are the charge-density wave (CDW) and spin-density wave (SDW) in high-temperature cuprate superconductors [1–4] and iron-based superconductors [5–9]. Recently, high-temperature superconductivity has been discovered in layered nickelates in Ruddlesden-Popper (RP) phase under moderately high pressure [10–15]. Likewise, density-wave states have been revealed in the phase diagram of both bilayer and trilayer nickelates in RP-phase at ambient pressure [10,12-14,16-21]. Apparently, the exploration of the density-wave states in RP-phase nickelates will not only provide important insights into their normal state properties but also help construct a unified picture of unconventional superconductivity.

Ultrafast laser pulses possess a unique capability to disentangle different degrees of freedom at ultrashort time scale and extract dynamic information about ordered states, including relaxation process, microscopic coupling nature, and energy gap dynamics [22]. Based on the pump–probe technique, time-resolved probes have been widely used to investigate the density waves in different systems [23–26], including many nickelate compounds. In particular, ultrafast optical spectroscopy has revealed rich intriguing dynamic behaviors of nickelate superconductors, such as photo-excited phase fluctuations preserving long-range order [27],

* Corresponding authors.
E-mail addresses: ligang@shanghaitech.edu.cn (G. Li), hjguo@sslab.org.cn (H. Guo), luyi-yang@mail.tsinghua.edu.cn (L. Yang), lxyang@tsinghua.edu.cn (L. Yang).

https://doi.org/10.1016/j.scib.2024.10.011

ultrafast charge localization and the dynamics of the pseudogap [28], vibrational symmetry breaking process [29], and the evidence for *d*-wave superconductivity [30].

In this work, by employing time-resolved reflectivity measurements, we systematically investigate the ultrafast dynamics of the bilayer and trilayer nickelates at ambient pressure. Despite their similar structure based on Ni-O layers, we observe drastic difference in their dynamic behaviors. The relaxation time of $La_4Ni_3O_{10}$ diverges around the density-wave transition temperature, suggesting an energy gap of about 16.7 ± 4.3 meV, which is in drastic contrast to the weak kink-like features in $La_3Ni_2O_7$. The ultrashort laser pulse excites a coherent phonon mode involving collective motions of La, Ni, and O atoms, which is absent in $La_3Ni_2O_7$. More importantly, the extracted electron–phonon coupling (EPC) constant in $La_4Ni_3O_{10}$ is more than twice the value in $La_3Ni_2O_7$, consistent with the difference in the relaxation time of the two systems. Our investigation advances the understanding of the normal-state properties of newly discovered high-temperature nickelate superconductors and sheds light on the unconventional superconductivity in nickelates.

2. Materials and methods

2.1. Crystal synthesis

Single crystals of $La_3Ni_2O_7$ and $La_4Ni_3O_{10}$ were grown by the high-pressure optical floating zone technique [31]. Raw materials of La_2O_3 (99.99%) were heated at 900 °C overnight to remove the undesired $La(OH)_3$ phase. Subsequently, La_2O_3 and NiO (99.99%) powders were mixed in a stoichiometric ratio with 1%–2% excess of NiO to compensate for its evaporation at high temperatures. The mixture was then pressed into pellets and sintered at 1100 °C in the air for 48 h with several intermediate grindings. The reactant was pressed into rods with a diameter of about 6 mm and a length of about 14 cm under hydrostatic pressure and then sintered at 1300 °C for 2 h. The single crystals of $La_3Ni_2O_7$ and $La_4Ni_3O_{10}$ were then grown in a high-pressure optical floating zone furnace (HKZ-300) with an oxygen pressure of 15 and 20 bar, respectively. The feed and seed rods were counter-rotated with speeds of 20 and 25 r min^{-1}, respectively. Growth rates of 2 and 5 mm h^{-1} were used for the $La_3Ni_2O_7$ and $La_4Ni_3O_{10}$ phases, respectively.

2.2. Tr-reflectivity measurements

Tr-reflectivity experiments were conducted using a Ti:sapphire oscillator with a center wavelength of 800 nm and a repetition rate of 80 MHz in a standard wavelength-degenerate pump–probe setup. Both the pump and probe beams are linearly polarized in a cross-polarization configuration to eliminate pump scattering. The pump and probe beams are focused to 26 and 12 μm on the sample, respectively. The intensity of the pump beam was modulated by an optical chopper at 3 kHz to facilitate lock-in detection. The overall temporal resolution is compressed to 40 fs using negative-dispersive mirrors. The reflectivity signal was detected by a balanced detector to mitigate laser power fluctuations. The sample was cleaved and subsequently kept in a cryostat under a vacuum of better than 1×10^{-3} mbar during experiments.

2.3. Raman spectroscopy

Raman spectra at room temperature were acquired in the backscattering geometry with a Jobin-Yvon HR800 Raman system equipped with a 532 nm diode-pumped-solid-state laser, a 100 × objective (numerical aperture = 0.9), and a liquid-nitrogen-cooled charge-coupled-device detector. Laser plasma lines were removed via BragGrate bandpass filters. High resolution of 0.32 cm^{-1} was achieved by employing a grating with 2400 lines per mm. Three BragGrate notch filters were strategically applied to enable the lowest frequency down to 5 cm^{-1}. Temperature-dependent Raman data were similarly acquired, albeit with variations. A 785 nm solid-state laser and a 50 × objective (numerical aperture = 0.55) were employed. An edge filter enabled the measurement down to 20 cm^{-1} and a grating with 1200 lines per mm was used to achieve the spectral resolution of 0.36 cm^{-1}. The experimental setup incorporated a Montana cryostat system to achieve low temperatures and maintained the sample under a vacuum of 0.1 mTorr (1 mTorr = 0.01333224 Pa).

2.4. Density-functional theory calculations

The density-functional-theory (DFT) calculations were performed using the Vienna Ab initio Simulation Package (VASP) [32]. The electronic correlations were described by the Perdew-Burke-Ernzernhof functional [33]. The plane-wave cutoff energy was chosen to be 500 eV. Concerning the Brillouin zone integration, we use a 7 × 7 × 2 Monkhorst-Pack *k*-grid (spacing between *k*-points is 0.18 $Å^{-1}$). Structural relaxation was performed with a conjugated-gradient algorithm until the Hellmann-Feynman forces on each atom were less than 1 meV $Å^{-1}$ and the total energy was less than 10^{-6} eV. To accelerate the calculation, we calculated the phonon dynamic matrix without expanding the primitive cell. The phonon spectrum and phonon eigenvectors were further obtained by using PHONOPY [34] with the frozen-phonon method.

3. Results and discussion

Fig. 1a and b compare the crystal structures of $La_3Ni_2O_7$ and $La_4Ni_3O_{10}$ at ambient pressure. In each unit cell, two (three) Ni-O layers form a bilayer (trilayer) structure by sharing apical oxygen atoms. Temperature-dependent resistivity of $La_3Ni_2O_7$ was manifested by the kink-like features (Fig. 1c), which were attributed to density-wave transitions [10,17]. However, it should be noted that the complicated structural imperfections of $La_3Ni_2O_7$, including the oxygen vacancies [35] and the intergrowth with other $La_3Ni_2O_7$ phases and $La_4Ni_3O_{10}$ [15, 36–38], may also induce the kink-like features in the transport measurements. By contrast, a well-defined CDW/SDW transition is revealed by a rapid increase of the resistivity near 132 K with decreasing temperature in $La_4Ni_3O_{10}$ (Fig. 1c), which is also evidenced by the cusp in the susceptibility and specific heat [39–42]. The resistivity then peaks near 120 K and decreases monotonically down to the lowest temperature. Fig. 1d compares the Raman spectra of $La_3Ni_2O_7$ and $La_4Ni_3O_{10}$ at room temperature. In the high-frequency range (200–600 cm^{-1}), the evident phonons locate near 564 cm^{-1} (16.92 THz) and 396 cm^{-1} (11.88 THz) in $La_3Ni_2O_7$ and $La_4Ni_3O_{10}$, respectively. Notably, $La_4Ni_3O_{10}$ exhibits more low-frequency phonons below 200 cm^{-1}, likely due to its more complicated trilayer structure and lower crystal symmetry, which allow more phonon modes [43,44].

Fig. 2 shows the prototypical transient change of the optical reflectivity, $\Delta R/R = [R(t) - R_0]/R_0$, where R_0 is the reflectivity measured before the pump pulse arrives. Overall, both the data of $La_3Ni_2O_7$ and $La_4Ni_3O_{10}$ show an instantaneous excitation followed by an exponential decay (Fig. 2a and b). By fitting the data at 80 K to a single-exponential decay (Supplementary materials, Figs. S2 and S3 online), we obtain relaxation time around 3.68 and 0.57 ps for $La_3Ni_2O_7$ and $La_4Ni_3O_{10}$, respectively. The difference in their relaxation time suggests distinct relaxation processes in the two systems, consistent with their different resistivity behaviors. Moreover, on top of the exponential decay, there is a periodic

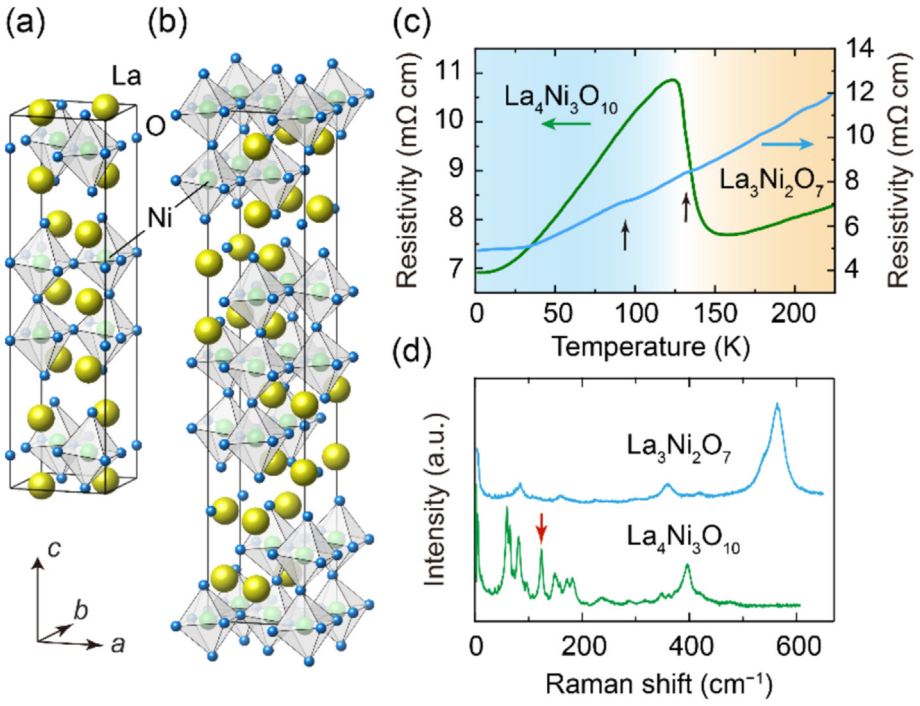

Fig. 1. Basic properties of $La_3Ni_2O_7$ and $La_4Ni_3O_{10}$. (a, b) Crystal structures of $La_3Ni_2O_7$ (a) and $La_4Ni_3O_{10}$ (b). (c) Temperature-dependent resistivity of $La_3Ni_2O_7$ (blue curve) and $La_4Ni_3O_{10}$ (green curve) at ambient pressure, black arrows indicate kink-like features in $La_3Ni_2O_7$. (d) 532 nm Raman spectra of $La_3Ni_2O_7$ and $La_4Ni_3O_{10}$, measured at room temperature.

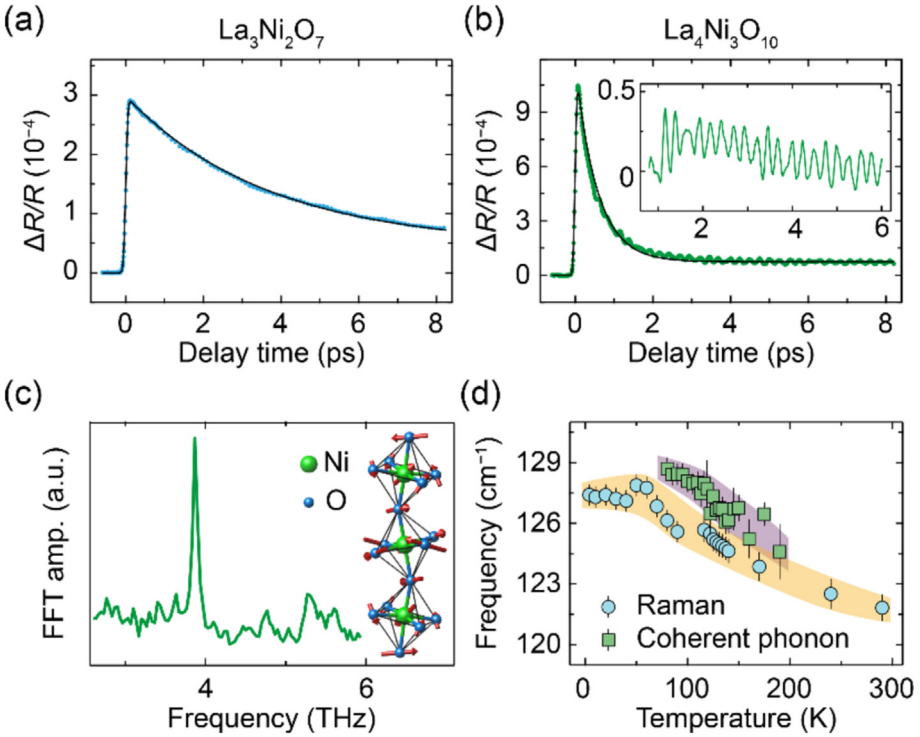

Fig. 2. Excitation of coherent phonons in $La_4Ni_3O_{10}$. (a) Transient reflectivity change $\Delta R/R$ of $La_3Ni_2O_7$ at 80 K. (b) $\Delta R/R$ of $La_4Ni_3O_{10}$ at 80 K showing the observation of coherent phonon vibrations. The inset shows the oscillatory part of the signal after subtracting the single-exponential background. (c) Fourier transform of the oscillating part of the signal, the most prominent phonon mode locates at 3.87 THz. The inset shows the corresponding vibration of the atoms with the red arrows indicating the vibration directions. For simplicity, La atoms vibrating mainly in the plane are not shown (see the Supplementary video). (d) Temperature-dependence of the coherent phonon frequency of $La_4Ni_3O_{10}$ measured using ultrafast reflectivity and Raman experiments. Data of the ultrafast reflectivity were collected at the pump fluence F = 7μJ cm^{-2}.

oscillation of the transient reflectivity of $La_4Ni_3O_{10}$ (inset of Fig. 2b), which is, however, absent in $La_3Ni_2O_7$.

The observation of the oscillation implies the excitation of coherent phonon modes, as evidenced by the Fourier transform of the oscillation data (Fig. 2c). With the help of DFT calculation, the most prominent phonon mode at 3.87 THz (129 cm^{-1}) is identified as the A_g mode involving collective motion of La, Ni, and O atoms (inset of Fig. 2c). Within the trilayer unit cell, the La atoms vibrate mainly in the plane. The outer Ni atoms exhibit both out-of-plane and in-plane vibration, while the inner Ni atoms stay put. The apical O atoms vibrate mainly in the plane, in contrast to the in-plane O atoms vibrating in both in-plane and out-of-plane directions (See Supplementary materials, Fig. S5 (online) and the Supplementary video for details). This phonon mode is also observed in the Raman data of $La_4Ni_3O_{10}$ but absent in $La_3Ni_2O_7$ (red arrow in Fig. 1d). Fig. 2d summarizes the temperature evolution of the frequency of the coherent phonon (the Supplementary materials), which gradually softens with increasing temperature.

Such a collective motion with A_g symmetry involving different vibrations of Ni-O atoms is, in principle, not possible in the bilayer $La_3Ni_2O_7$ due to the symmetry limitation. On the other hand, as inspired by the unique SDW state in $La_4Ni_3O_{10}$, where only the outer Ni-O layers show a periodic modulation of the spin moment [39], we propose that the excited coherent phonon with distinct motion of the three Ni-O layers may provide a coherent manipulation of the SDW order in $La_4Ni_3O_{10}$.

Fig. 3 explores the temperature evolution of the ultrafast optical reflectivity. The false-color plots of the transient reflectivity of $La_3Ni_2O_7$ and $La_4Ni_3O_{10}$ in Fig. 3a and b reveal clear difference in their temperature-dependent behaviors. The relaxation time of $La_3Ni_2O_7$ is continuously prolonged as the temperature decreases. However, it increases abruptly near the density-wave transition temperature in $La_4Ni_3O_{10}$, in line with the previous observations in various density-wave materials [45–48]. The different temperature dependence of the dynamics in the two nickelates is further evidenced by the transient reflectivity change at selected temperatures shown in Fig. 3c and d.

To quantify the change of the dynamics across the CDW/SDW transition, we extract the amplitudes A and relaxation times τ of the transient reflectivity change $\Delta R/R$ by fitting the data to a single-exponential decay (Supplementary materials, Figs. S2 and S3 (online). Fig. 4 summarizes the results as functions of the temperature and the pump fluence. In $La_3Ni_2O_7$, both A and τ decrease monotonically with the elevated temperature. We note the changes of the slope of A and τ (Fig. 4a and b), which may be related to the kink-like features in the resistivity and other transport measurements (black arrows in Fig. 1c) [31,39]. Interestingly, we observe a linear temperature-dependence of the scattering rate $1/\tau$ as shown in the inset of Fig. 4b, which suggests a non-Fermi liquid behavior of the system, consistent with the previous optical spectroscopy experiment [49].

The results in $La_4Ni_3O_{10}$ are qualitatively different from $La_3Ni_2O_7$. The amplitude shows a dip and the relaxation time shows a profound divergence near the CDW/SDW transition temperature (Fig. 4c, d, and the Supplementary materials). This divergent behavior has been widely observed in density-wave materials

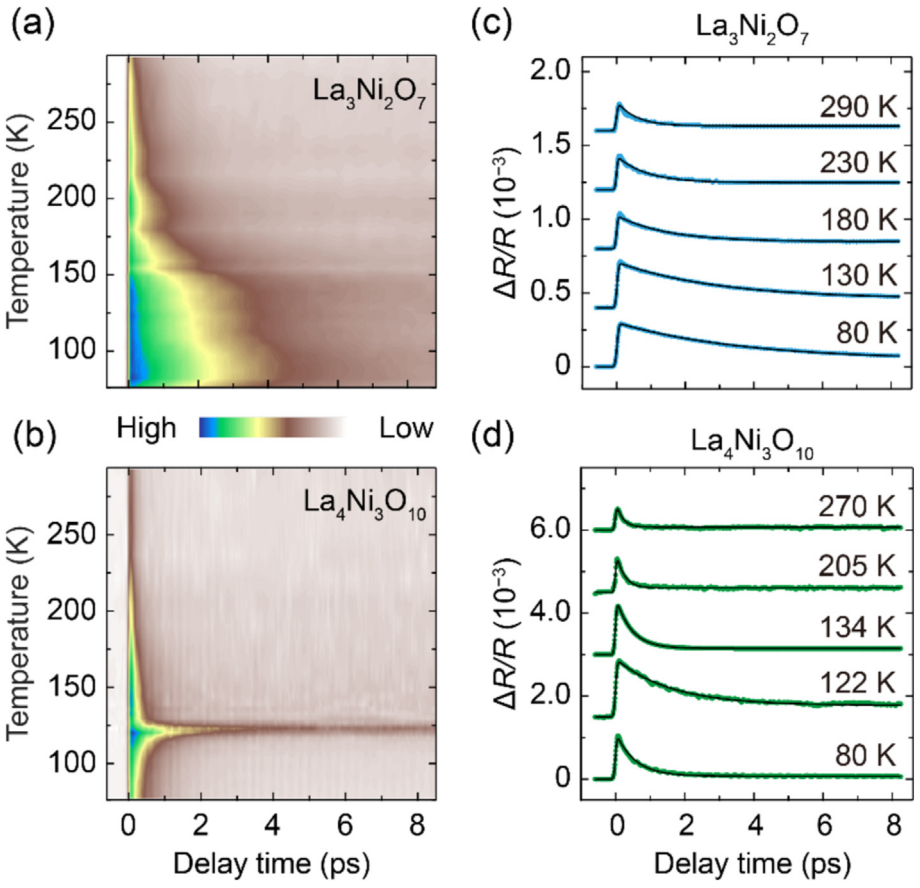

Fig. 3. Temperature-dependent transient reflectivity change $\Delta R/R$. (a, b) The false-color plot of temperature-dependent transient reflectivity data of $La_3Ni_2O_7$ (a) and $La_4Ni_3O_{10}$ (b). (c, d) Typical temporal evolution of $\Delta R/R$ in $La_3Ni_2O_7$ (c) and $La_4Ni_3O_{10}$ (d) at selected temperatures. The black curves are the phenomenological fit of the data. Data were collected at the pump fluence F = 7 μJ cm^{-2}.

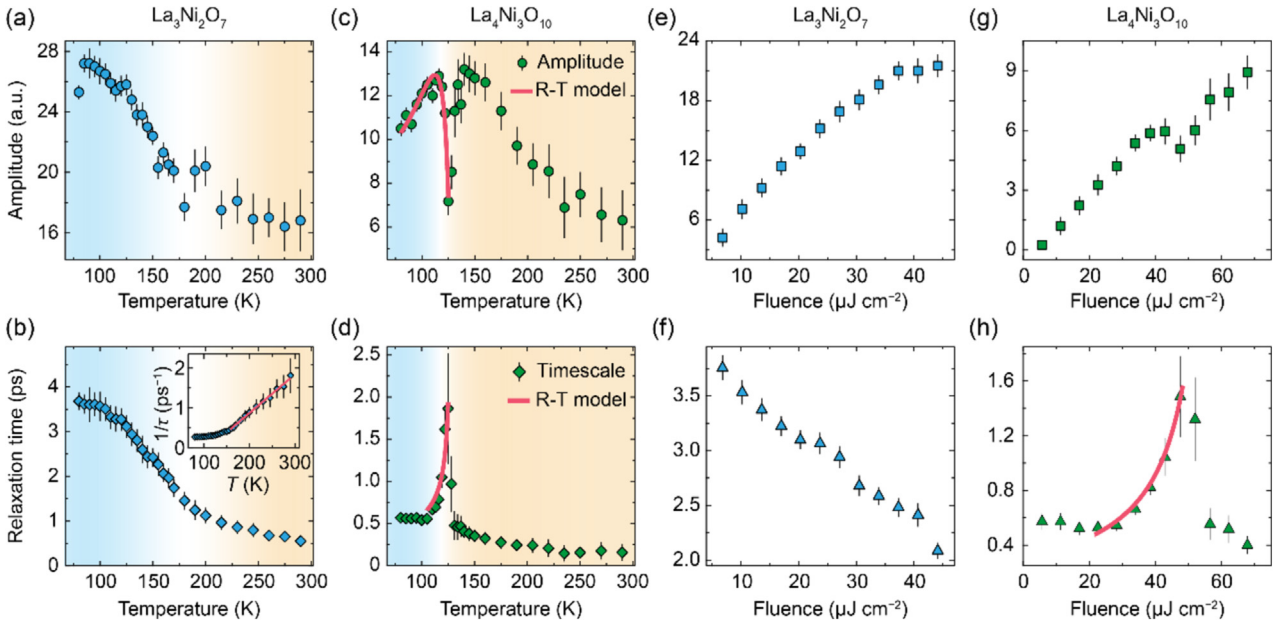

Fig. 4. Evolution of the amplitude A and relaxation time τ of transient reflectivity change. (a, b) Temperature dependence of A (a) and τ (b) extracted in $La_3Ni_2O_7$. The inset of panel (b) shows the temperature dependence of $1/\tau$. (c, d) The same as (a) and (b) but for $La_4Ni_3O_{10}$. The red curves are the fit of the data to the Rothwarf-Taylor (R-T) model. Data in (a–d) were collected at the pump fluence F = 7 μJ cm^{-2}. (e, f) Fluence dependence of A (e) and τ (f) extracted in $La_3Ni_2O_7$. (g, h) The same as (e) and (f) but for $La_4Ni_3O_{10}$. The red curve in (h) is the fit of the data (see the main text). Data in (e–h) were measured at 80 K.

[45–48], which can be understood within the Rothwarf-Taylor (R-T) model aiming to elucidate the bottleneck effect caused by an energy gap [50]. The nice conformity between our data and the R-T model confirms the prototypical gap dynamics in the CDW/SDW state of $La_4Ni_3O_{10}$. By fitting the model to our data in Fig. 4c and d, we obtain an energy gap of Δ_0 = 16.7 ± 4.3 meV (the Supplementary materials), in good agreement with the previous angle-resolved photoemission spectroscopy (ARPES) measurement [51,52]. In $La_3Ni_2O_7$, although a gap of about 50 meV was reported in the Ni-d_{z^2} band in the optical spectroscopy measurement of $La_3Ni_2O_7$ [49], a well-defined density-wave gap is elusive in the ARPES [53,54], and the density-wave transition is absent in the ultrafast experiment here.

We further estimate the EPC constant λ based on the relation $\tau = \pi k_B T_e / 3\hbar\lambda\langle\omega^2\rangle$ [55–58], where k_B and $\hbar$ are Boltzmann and reduced Planck constant, respectively, $\lambda\langle\omega^2\rangle$ is the second moment of the Eliashberg function, and T_e is the electron temperature estimated with the two-temperature model [55,56]. Using this simple model, we obtain $\lambda\langle\omega^2\rangle$ = 37.78 meV^2 and $\lambda\langle\omega^2\rangle$ = 123.55 meV^2 for $La_3Ni_2O_7$ and $La_4Ni_3O_{10}$, respectively (the Supplementary materials). After initial thermalization, the interaction with Debye phonons is the most efficient channel for the relaxation of hot carriers. It is therefore reasonable and commonly used to estimate $\langle\omega^2\rangle$ using Debye phonons, that is, $\langle\omega^2\rangle \propto \Theta_D^2$ [59–61], where Θ_D is the Debye temperature. With Θ_D = 383 K (33.0 meV) [62] and Θ_D = 459 K (39.6 meV) [12] for $La_3Ni_2O_7$ and $La_4Ni_3O_{10}$, we obtain λ = 0.05–0.07 and λ = 0.12–0.16, respectively (the Supplementary materials). These values are consistent with the rough estimation using $\lambda \approx \hbar/\tau\Omega_D$ = 0.04 and 0.11 for $La_3Ni_2O_7$ and $La_4Ni_3O_{10}$, respectively, where Ω_D is the Debye frequency [63]. The EPC constant of $La_4Ni_3O_{10}$ agrees well with the value of λ = 0.124 given by the transport experiment [42] and those in other nickelates [64]. It is noteworthy that the estimated weak EPC constant at ambient pressure should not completely exclude the role of EPC in the high-temperature superconductivity at high pressure. Recent calculations have predicted an enhanced EPC constant as large as 1.75 in pressurized $La_3Ni_2O_7$ [65], which requires further experimental investigations.

Finally, we show the results measured under different pump fluences (F) at 80 K in Fig. 4e–h. Due to the increased photo-excited carriers, the amplitude of $\Delta R/R$ linearly increases with the pump fluence in $La_3Ni_2O_7$, with a signature of saturation or change of the slope at high-fluence regime (the damage threshold for $La_3Ni_2O_7$ crystals is about 100 μJ cm^{-2}) (Fig. 4e). Similar to the temperature-dependent experiments in Fig. 4b, the relaxation time continuously decreases with the pump fluence. In $La_4Ni_3O_{10}$, however, we observe a clear anomaly near 48 μJ cm^{-2} in both the amplitude and relaxation time. In particular, the fluence-dependent relaxation time drastically increases at 48 μJ cm^{-2}, which fits nicely to the assumption that the relaxation time is inversely proportional to the gap Δ and the gap is suppressed by ultrashort laser pulse according to $\Delta = \Delta_0(1 - F/F_T)$ (red curve in Fig. 4h) [66], where F_T is the threshold fluence required to suppress the density-wave order. The threshold fluence of 48 μJ cm^{-2} corresponds to about 5.4 meV per unit cell, about one order larger than the electronic condensation energy of $N(E_F)\Delta^2/2 \approx$ 0.42 meV, where $N(E_F)$ is the electronic density of states at E_F. This observation is on contrary to the results in the excitonic CDW material $TiSe_2$ [67] but in line with those in the prototypical Peierls CDW material $(K, Rb)_{0.3}MoO_3$, where a large amount of photon energy is deposited to the lattice [23,68].

4. Conclusion

In summary, we present a comprehensive ultrafast optical reflectivity study of $La_3Ni_2O_7$ and $La_4Ni_3O_{10}$. While $La_4Ni_3O_{10}$ exhibits a prototypical density-wave dynamics, $La_3Ni_2O_7$ shows a weak transition-like behavior with a non-Fermi liquid behavior at high temperatures, suggesting a drastic difference in the density-wave states of the two compounds. Moreover, we observe the excitation

of coherent phonon modes involving different vibrations of the three Ni-O layers in $La_4Ni_3O_{10}$, which may provide a route to coherently control the magnetism of the system. Our findings provide dynamic information on the interplay of multiple degrees of freedom in the nickelates, which will deepen our understanding of the normal state and superconducting properties of Ni-based high-temperature superconductors.

Note: *During the preparation of the manuscript, we noted two independent works about the ultrafast dynamics of* $La_3Ni_2O_7$ [69] *and* $La_4Ni_3O_{10}$ [70] *with consistent results.*

Conflict of interest

The authors declare that they have no conflict of interest.

Acknowledgments

This work is funded by the National Key R&D Program of China (2022YFA1403100, 2022YFA1403201, and 2022YFA1402703), the National Natural Science Foundation of China (12274251, 92365204, 12004270, 52272265, 12361141826, and 12074212), and the Guangdong Basic and Applied Basic Research Foundation (2022B1515120020). Lexian Yang acknowledges support from the Tsinghua University Initiative Scientific Research Program and the Fund of Science and Technology on Surface Physics and Chemistry Laboratory (XKFZ202102). Gang Li acknowledges the support of 2021-Fundamental Research Area 21JC1404700, and Sino-German Mobility program (M-0006). Luyi Yang acknowledges the support of the Beijing Natural Science Foundation (Z240006).

Author contributions

Lexian Yang and Luyi Yang conceived the experiments. Yidian Li carried out ultrafast reflectivity measurements with the assistance of Liangyang Liu, Pai Peng, Hao Lin, Xian Du, Wenxuan Zhao, Kaiyi Zhai, Luyi Yang, and Lexian Yang. *Ab-initio* calculations were performed by Xuefeng Zhang and Gang Li. Single crystals were synthesized and characterized by Yantao Cao, Cuiying Pei, Mingxin Zhang, Jinkui Zhao, Yanpeng Qi, and Hanjie Guo. Yidian Li and Heng Wu carried out Raman measurements with the guidance of Miaoling Lin and Pingheng Tan. The paper was written by Yidian Li, Luyi Yang, and Lexian Yang. All authors contributed to the scientific planning, discussion, and manuscript revision.

Appendix A. Supplementary material

Supplementary data to this article can be found online at https://doi.org/10.1016/j.scib.2024.10.011.

References

[1] Fradkin E, Kivelson SA, Tranquada JM. Colloquium: theory of intertwined orders in high temperature superconductors. Rev Mod Phys 2015;87:457–82.
[2] Tranquada JM, Sternlieb BJ, Axe JD, et al. Evidence for stripe correlations of spins and holes in copper oxide superconductors. Nature 1995;375:561–3.
[3] Ghiringhelli G, Le Tacon M, Minola M, et al. Long-range incommensurate charge fluctuations in (Y, Nd)$Ba_2Cu_3O_{6+x}$. Science 2012;337:821–5.
[4] da Silva Neto EH, Aynajian P, Frano A, et al. Ubiquitous interplay between charge ordering and high-temperature superconductivity in cuprates. Science 2014;343:393–6.
[5] Dai PC. Antiferromagnetic order and spin dynamics in iron-based superconductors. Rev Mod Phys 2015;87:855–96.
[6] Ge QQ, Ye ZR, Xu M, et al. Anisotropic but nodeless superconducting gap in the presence of spin-density wave in iron-pnictide superconductor $NaFe_{1-x}Co_xAs$. Phys Rev X 2013;3:011020.
[7] Allred JM, Taddei KM, Bugaris DE, et al. Double-Q spin-density wave in iron arsenide superconductors. Nat Phys 2016;12:493–8.
[8] Chen GF, Li Z, Wu D, et al. Superconductivity at 41 K and its competition with spin-density-wave instability in layered $CeO_{1-x}F_xFeAs$. Phys Rev Lett 2008;100:247002.
[9] Zhou XD, Cai P, Wang AF, et al. Evolution from unconventional spin density wave to superconductivity and a pseudogaplike phase in $NaFe_{1-x}Co_xAs$. Phys Rev Lett 2012;109:037002.
[10] Sun HL, Huo MW, Hu XW, et al. Signatures of superconductivity near 80 K in a nickelate under high pressure. Nature 2023;621:493–8.
[11] Sakakibara H, Ochi M, Nagata H, et al. Theoretical analysis on the possibility of superconductivity in the trilayer Ruddlesden-Popper nickelate $La_4Ni_3O_{10}$ under pressure and its experimental examination: comparison with $La_3Ni_2O_7$. Phys Rev B 2024;109:144511.
[12] Zhang MX, Pei CY, Du X, et al. Superconductivity in trilayer nickelate $La_4Ni_3O_{10}$ under pressure. arXiv: 2311.07423, 2023.
[13] Li Q, Zhang YJ, Xiang ZN, et al. Signature of superconductivity in pressurized $La_4Ni_3O_{10}$. Chin Phys Lett 2024;41:017401.
[14] Zhu Y, Peng D, Zhang E, et al. Superconductivity in pressurized trilayer $La_4Ni_3O_{10-\delta}$ single crystals. Nature 2024;631:531–6.
[15] Wang NN, Wang G, Shen XL, et al. Bulk high-temperature superconductivity in the high-pressure tetragonal phase of bilayer $La_2PrNi_2O_7$. Nature 2024;634:579–84.
[16] Zhang MX, Pei CY, Wang Q, et al. Effects of pressure and doping on Ruddlesden-Popper phases $La_{n+1}Ni_nO_{3n+1}$. J Mater Sci Technol 2024;185:147–54.
[17] Zhang YN, Su DJ, Huang YN, et al. High-temperature superconductivity with zero resistance and strange-metal behaviour in $La_3Ni_2O_{7-\delta}$. Nat Phys 2024;20:1269–73.
[18] Dan Z, Zhou YB, Huo MW, et al. Spin-density-wave transition in double-layer nickelate $La_3Ni_2O_7$. arXiv: 2402.03952, 2024.
[19] Chen XY, Choi J, Jiang ZC, et al. Electronic and magnetic excitations in $La_3Ni_2O_7$. arXiv: 2401.12657, 2024.
[20] Zhou YZ, Guo J, Cai S, et al. Evidence of filamentary superconductivity in pressurized $La_3Ni_2O_7$ single crystals. arXiv: 2311.12361, 2023.
[21] Wang G, Wang NN, Shen XL, et al. Pressure-induced superconductivity in polycrystalline $La_3Ni_2O_{7-\delta}$. Phys Rev X 2024;14:011040.
[22] de la Torre A, Kennes DM, Claassen M, et al. Colloquium: nonthermal pathways to ultrafast control in quantum materials. Rev Mod Phys 2021;93:041002.
[23] Yang LX, Rohde G, Hanff K, et al. Bypassing the structural bottleneck in the ultrafast melting of electronic order. Phys Rev Lett 2020;125:266402.
[24] Yang LX, Rohde G, Rohwer T, et al. Ultrafast modulation of the chemical potential in $BaFe_2As_2$ by coherent phonons. Phys Rev Lett 2014;112:207001.
[25] Rohwer T, Hellmann S, Wiesenmayer M, et al. Collapse of long-range charge order tracked by time-resolved photoemission at high momenta. Nature 2011;471:490–3.
[26] Schmitt F, Kirchmann PS, Bovensiepen U, et al. Transient electronic structure and melting of a charge density wave in $TbTe_3$. Science 2008;321:1649–52.
[27] Lee WS, Chuang YD, Moore RG, et al. Phase fluctuations and the absence of topological defects in a photo-excited charge-ordered nickelate. Nat Commun 2012;3:838.
[28] Coslovich G, Huber B, Lee WS, et al. Ultrafast charge localization in a stripe-phase nickelate. Nat Commun 2013;4:2643.
[29] Coslovich G, Kemper AF, Behl S, et al. Ultrafast dynamics of vibrational symmetry breaking in a charge-ordered nickelate. Sci Adv 2017;3:e1600735.
[30] Cheng B, Cheng D, Lee K, et al. Evidence for *d*-wave superconductivity of infinite-layer nickelates from low-energy electrodynamics. Nat Mater 2024;23:775–81.
[31] Liu ZJ, Sun HL, Huo MW, et al. Evidence for charge and spin density waves in single crystals of $La_3Ni_2O_7$ and $La_3Ni_2O_6$. Sci China Phys Mech Astro 2022;66:217411.
[32] Kresse G, Furthmüller J. Efficiency of ab-initio total energy calculations for metals and semiconductors using a plane-wave basis set. Comp Mater Sci 1996;6:15–50.
[33] Perdew JP, Burke K, Ernzerhof M. Generalized gradient approximation made simple. Phys Rev Lett 1996;77:3865–8.
[34] Togo A, Tanaka I. First principles phonon calculations in materials science. Scripta Mater 2015;108:1–5.
[35] Dong ZH, Huo MW, Li J, et al. Visualization of oxygen vacancies and self-doped ligand holes in $La_3Ni_2O_{7-\delta}$. Nature 2024;630:847–52.
[36] Puphal P, Reiss P, Enderlein N, et al. Unconventional crystal structure of the high-pressure superconductor $La_3Ni_2O_7$. arXiv: 2312.07341, 2023.
[37] Chen XL, Zhang JJ, Thind AS, et al. Polymorphism in the Ruddlesden-Popper nickelate $La_3Ni_2O_7$: discovery of a hidden phase with distinctive layer stacking. J Am Chem Soc 2024;146:3640–5.
[38] Xie T, Huo MW, Ni XS, et al. Strong interlayer magnetic exchange coupling in $La_3Ni_2O_{7-\delta}$ revealed by inelastic neutron scattering. Sci Bull 2024;69:3221–7.
[39] Zhang J, Phelan D, Botana AS, et al. Intertwined density waves in a metallic nickelate. Nat Commun 2020;11:6003.
[40] Rout D, Mudi SR, Hoffmann M, et al. Structural and physical properties of trilayer nickelates $R_4Ni_3O_{10}$ (R = La, Pr, and Nd). Phys Rev B 2020;102:195144.
[41] Zhang Z, Greenblatt M. Synthesis, structure, and properties of $Ln_4Ni_3O_{10-\delta}$ (Ln = La, Pr, and Nd). J Solid State Chem 1995;117:236–46.
[42] Kumar S, Fjellvåg Ø, Sjåstad AO, et al. Physical properties of Ruddlesden-Popper (n = 3) nickelate: $La_4Ni_3O_{10}$. J Magn Magn Mater 2020;496:165915.

[43] Zhan J, Gu YH, Wu XX, et al. Cooperation between electron-phonon coupling and electronic interaction in bilayer nickelates $La_3Ni_2O_7$. arXiv: 2404.03638,2024.
[44] LaBollita H, Kapeghian J, Norman MR, et al. Electronic structure and magnetic tendencies of trilayer $La_4Ni_3O_{10}$ under pressure: structural transition, molecular orbitals, and layer differentiation. Phys Rev B 2024;109:195151.
[45] Demsar J, Biljaković K, Mihailovic D. Single particle and collective excitations in the one-dimensional charge density wave solid $K_{0.3}MoO_3$ probed in real time by femtosecond spectroscopy. Phys Rev Lett 1999;83:800–3.
[46] Yusupov RV, Mertelj T, Chu JH, et al. Single-particle and collective mode couplings associated with 1- and 2-directional electronic ordering in metallic RTe_3 (R = Ho, Dy, Tb). Phys Rev Lett 2008;101:246402.
[47] Li RS, Yue L, Wu Q, et al. Optical spectroscopy and ultrafast pump-probe study of a quasi-one-dimensional charge density wave in CuTe. Phys Rev B 2022;105:115102.
[48] Borovšak M, Stojchevska L, Sutar P, et al. Critical femtosecond relaxation dynamics of collective and single-particle excitations through the phase transitions in single crystals of η-Mo_4O_{11}. Phys Rev B 2016;93:125123.
[49] Liu Z, Huo M, Li J, et al. Electronic correlations and partial gap in the bilayer nickelate $La_3Ni_2O_7$. Nat Commun 2024;15:7570.
[50] Rothwarf A, Taylor BN. Measurement of recombination lifetimes in superconductors. Phys Rev Lett 1967;19:27–30.
[51] Li H, Zhou X, Nummy T, et al. Fermiology and electron dynamics of trilayer nickelate $La_4Ni_3O_{10}$. Nat Commun 2017;8:704.
[52] Du X, Li YD, Cao YT, et al. Correlated electronic structure and density-wave gap in trilayer nickelate $La_4Ni_3O_{10}$. arXiv: 2405.19853, 2024.
[53] Yang JG, Sun HL, Hu XW, et al. Orbital-dependent electron correlation in double-layer nickelate $La_3Ni_2O_7$. Nat Commun 2024;15:4373.
[54] Li YD, Du X, Cao YT, et al. Electronic correlation and pseudogap-like behavior of high-temperature superconductor $La_3Ni_2O_7$. Chin Phys Lett 2024;41:087402.
[55] Luo CW, Wu IH, Cheng PC, et al. Quasiparticle dynamics and phonon softening in FeSe superconductors. Phys Rev Lett 2012;108:257006.
[56] Mansart B, Boschetto D, Savoia A, et al. Ultrafast transient response and electron-phonon coupling in the iron-pnictide superconductor $Ba(Fe_{1-x}Co_x)_2As_2$. Phys Rev B 2010;82:024513.
[57] Avigo I, Cortés R, Rettig L, et al. Coherent excitations and electron–phonon coupling in $Ba/EuFe_2As_2$ compounds investigated by femtosecond time- and angle-resolved photoemission spectroscopy. J Phys: Condens Matter 2013;25:094003.
[58] Kabanov VV, Alexandrov AS. Electron relaxation in metals: theory and exact analytical solutions. Phys Rev B 2008;78:174514.
[59] Papaconstantopoulos DA, Boyer LL, Klein BM, et al. Calculations of the superconducting properties of 32 metals with $Z\leq49$. Phys Rev B 1977;15:4221–6.
[60] Lin Z, Zhigilei LV, Celli V. Electron-phonon coupling and electron heat capacity of metals under conditions of strong electron-phonon nonequilibrium. Phys Rev B 2008;77:075133.
[61] Lai Y-P, Chen H-J, Wu K-H, et al. Temperature-dependent carrier–phonon coupling in topological insulator Bi_2Se_3. Appl Phys Lett 2014;105:232110.
[62] Wu G, Neumeier JJ, Hundley MF. Magnetic susceptibility, heat capacity, and pressure dependence of the electrical resistivity of $La_3Ni_2O_7$ and $La_4Ni_3O_{10}$. Phys Rev B 2001;63:245120.
[63] Taneda T, Pepe GP, Parlato L, et al. Time-resolved carrier dynamics and electron-phonon coupling strength in proximized weak ferromagnet-superconductor nanobilayers. Phys Rev B 2007;75:174507.
[64] Meier QN, de Vaulx JB, Bernardini F, et al. Preempted phonon-mediated superconductivity in the infinite-layer nickelates. Phys Rev B 2024;109:184505.
[65] E.F. Talantsev, Chistyakov VV. Debye temperature, electron-phonon coupling constant, and microcrystalline strain in highly-compressed $La_3Ni_2O_{7-\delta}$. arXiv: 2401.00804, 2024.
[66] Wang ZX, Wu Q, Yin QW, et al. Unconventional charge density wave and photoinduced lattice symmetry change in the kagome metal CsV_3Sb_5 probed by time-resolved spectroscopy. Phys Rev B 2021;104:165110.
[67] Möhr-Vorobeva E, Johnson SL, Beaud P, et al. Nonthermal melting of a charge density wave in $TiSe_2$. Phys Rev Lett 2011;107:036403.
[68] Tomeljak A, Schäfer H, Städter D, et al. Dynamics of photoinduced charge-density-wave to metal phase transition in $K_{0.3}MoO_3$. Phys Rev Lett 2009;102:066404.
[69] Meng YH, Yang Y, Sun HL, et al. Density-wave-like gap evolution in $La_3Ni_2O_7$ under high pressure revealed by ultrafast optical spectroscopy. arXiv: 2404.19678, 2024.
[70] Xu SX, Chen CQ, M.W. H, et al. Origin of the density wave instability in trilayer nickelate $La_4Ni_3O_{10}$ revealed by optical and ultrafast spectroscopy. arXiv: 2405.19161, 2024.